EPJ Web of Conferences **380**, 02021 (2026) https://doi.org/10.1051/epjconf/202638002021
ICISCT'25

Robust Control Under External Disturbances for Grid Tied Solar Generator : a Comparative Study

Mina Elfarsaoui[1,*], *Ibtissam* Lachkar[1], *Abdelmajid* Abouloifa[1], *Elhoussin* Elbouchikhi[2], *Chaouqi* Aouadi[1], and *Abdelali* El Aroudi[3]

[1]ESE Laboratory, ENSEM, Hassan II University of Casablanca, Morocco
[2]ISEN Yncréa Ouest, Nantes, France
[3]Department d'Enginyeria Electronica, University Rovira i Virgili, Spain

Abstract. This paper investigates a three-phase grid-connected photovoltaic system equipped with battery storage and controlled through three different schemes: a conventional Proportional–Integral controller, a Twin Delayed Deep Deterministic Policy Gradient-based control method, and Linear Active Disturbance Rejection Control. Cascaded voltage and current loops are designed for the PV boost converter, the grid-side inverter, and the battery converter. The control system is required to maintain the PV array at its maximum power point, regulate the DC-link voltage, ensure sinusoidal grid currents with unity power factor, and impose a constant battery charging current. The three approaches are implemented under the same operating conditions and examined for irradiance variations. Their tracking and regulation performances are compared using numerical simulations developed in MATLAB/Simscape.

1 Introduction

The growth of renewable energy is part of a worldwide context in which efforts are being made to reduce greenhouse gas emissions and combat climate change. Faced with the depletion of fossil fuels and the high price of conventional sources, the power generation sector is looking for sustainable alternatives like photovoltaic solar power [1, 2].

Photovoltaic installations are generally divided into three main configurations. Standalone PV systems rely on battery storage to supply electricity to remote or isolated locations. Grid-connected systems deliver the generated power directly to the utility network. Hybrid PV systems combine grid connection with additional sources or storage devices, such as batteries, generator sets, or wind turbines, which improves autonomy and operating flexibility during power outages or periods of high demand [3].

Grid-connected PV systems require efficient control strategies to ensure optimal energy injection, system stability and conformity with power quality standards. Various control approaches have been developed, ranging from conventional methods to advanced and intelligent techniques [4]. Proportional-integral (PI) controllers are characterized by their simplicity, ease of implementation and steady-state efficiency. However, these controllers have limitations when systems are nonlinear [5]. To overcome the limitations of conventional

*e-mail: mina.elfarsaoui@ensem.ac.ma

methods, advanced control techniques have been introduced. Backstepping control [6], sliding mode control (SMC) [7] and active disturbance control (ADRC) [8], offer improved dynamic response and robustness. Model Predictive Control (MPC) [9] generally outperform advanced controllers when it comes to managing dynamically constrained multi-variable systems, thanks to their ability to anticipate and optimize system behavior over a predictive horizon; however, advanced controllers retain the advantage in terms of robustness, ease of real-time implementation, and reduced dependence on system model. Compared to advanced strategies and MPC, intelligent controls such as fuzzy logic [10], artificial neural networks (ANNs) [11], and reinforcement learning (RL) [12] offer dynamic adaptation to unmodeled uncertainties and disturbances, without requiring precise knowledge of the mathematical model of the system. Adaptive control represents a compromise between conventional or advanced approaches and intelligent methods, providing real-time updating of controller parameters in response to system variations [13, 14].

This study provides a comparative assessment of three control techniques: a conventional PI compensator, a PI controller combined with reinforcement learning, and a sliding mode controller. The proposed controllers are developed to achieve four main objectives: i) maximizing the power extracted from the photovoltaic panels, ii) injecting sinusoidal currents synchronized with the grid voltage, iii) maintaining the DC-link voltage at its reference value, and iv) ensuring constant-current battery charging.

The remainder of this article is organized as follows. Sect. 2 describes the overall configuration of the power conversion system and develops its mathematical model. Sect. 3 presents the controller design based on the three control strategies considered in this work. The simulation results and the comparative assessment of the control performance are provided in Sect. 4. Finally, Sect. 5 summarizes the main conclusions of the study.

2 Photovoltaic System Modeling

The configuration considered in this study is depicted in Figure 1. It combines a photovoltaic array with a DC/DC boost stage, a three-phase grid-side inverter, and a battery interfaced through a buck converter.

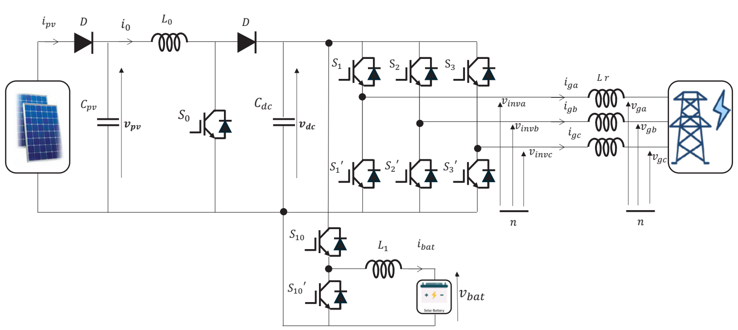

Figure 1. Overall configuration of the grid-connected photovoltaic system.

Using Kirchhoff's laws for the circuit shown in Fig. 1, the averaged model in the dq reference frame is written as follows:

$$C_{pv}\frac{d\bar{v}_{pv}}{dt} = \bar{i}_{pv} - \bar{i}_0 \tag{1}$$

$$L_0 \frac{d\bar{i}_0}{dt} = \bar{v}_{pv} - (1 - u_0)\bar{v}_{dc} \tag{2}$$

$$C_{dc} \frac{d\bar{v}_{dc}^2}{2dt} = \bar{v}_{pv}\bar{i}_{pv} - v_{bat}\bar{i}_{bat} - v_{gq}\bar{i}_{gq} \tag{3}$$

$$L \frac{d\bar{i}_{gd}}{dt} = L\omega\bar{i}_{gq} - r\bar{i}_{gd} + \frac{\bar{v}_{dc}}{2} u_d \tag{4}$$

$$L \frac{d\bar{i}_{gq}}{dt} = -L\omega\bar{i}_{gd} - r\bar{i}_{gq} - v_{gq} + \frac{\bar{v}_{dc}}{2} u_q \tag{5}$$

$$L_1 \frac{d\bar{i}_{bat}}{dt} = u_1\bar{v}_{dc} - v_{bat} \tag{6}$$

Here, $\bar{v}_{pv}$ and $\bar{i}_{pv}$ refer to the PV-array voltage and current. The inductor currents associated with L_0 and L_1 are denoted by $\bar{i}_0$ and i_{bat}, respectively. The quantities v_{bat} and $\bar{v}_{dc}$ represent the battery and DC-link voltages, while ω is the grid angular frequency. The rotating dq frame is oriented along the grid-voltage vector, with the q-axis chosen as the aligned axis; hence, $v_{gd} = 0$. Finally, u_0, u_1, u_d, and u_q are the control variables.

3 Controllers Design

The proposed control architecture is developed to satisfy the following objectives:

i) Operation of the PV array at its maximum power point by adjusting the DC/DC converter;

ii) Control of the grid-side converter to impose a sinusoidal current aligned with the grid voltage, corresponding to unity-power-factor operation (PFC);

iii) Regulation of the DC-link voltage at its prescribed reference value;

iv) Supply of a regulated constant current to the battery during charging.

Three control strategies are developed and evaluated, as summarized in Table 1: a conventional PI controller, a PI controller tuned using DRL, and LADRC. A cascaded voltage–current control scheme is implemented on both the PV and grid sides to improve the dynamic response of the overall system. In this configuration, the outer loop is responsible for voltage regulation, while the inner loop governs the current. This arrangement contributes to improving closed-loop stability while separating the fast current dynamics from the slower voltage dynamics.

Table 1. Control methods adopted for the defined objectives.

Objective	Approaches		
	PI	PI-RL	ADRC
MPPT	✓	✓	✓
PFC	✓	✓	✓
DC-link regulation	✓	✓	✓
Battery charging	✓	✗	✗

3.1 PI compensator

The mathematical model indicates that the system is nonlinear. Therefore, a small-signal linearization is performed before designing the linear PI compensator.

3.1.1 Current loops regulation

Based on Eqs. (2), (4), (5), and (6), the following control laws are applied:

$$
\begin{aligned}
u_0 &= 1 + \frac{k_0(\bar{i}_0^* - \bar{i}_0) - \bar{v}_{pv}}{\bar{v}_{dc}}, && (7)\\
u_d &= \frac{2}{\bar{v}_{dc}}\left(k_{p_{dq}}\left(e_{id} + \frac{r}{L}\int e_{id}dt\right) - L\omega\bar{i}_{gq}\right), && (8)\\
u_q &= \frac{2}{\bar{v}_{dc}}\left(k_{p_{dq}}\left(e_{iq} + \frac{r}{L}\int e_{iq}dt\right) + L\omega\bar{i}_{gd} + v_{gq}\right), && (9)\\
u_1 &= \frac{k_{bat}(\bar{i}_{bat}^* - \bar{i}_{bat}) + v_{bat}}{\bar{v}_{dc}}, && (10)
\end{aligned}
$$

where k_0, k_{dq}, and k_{bat} denote the proportional gains of controllers. The d- and q-axis current tracking errors are defined, respectively, as

$$e_{id} = \bar{i}_{gd}^* - \bar{i}_{gd}; \qquad e_{iq} = \bar{i}_{gq}^* - \bar{i}_{gq}$$

The closed-loop dynamics of the current control loops are described by the following transfer function:

$$Hc(s) = \frac{1}{1+\tau s} \tag{11}$$

The time constant τ is selected to determine the rapidity of current's loops. Its expressions, for each loop, are given as follows:

$$\tau = \begin{cases} \frac{L_0}{k_0} & \text{for } \bar{i}_0 \text{ loop} \\ \frac{L}{k_{p_{dq}}} & \text{for } \bar{i}_{gd}, \bar{i}_{gq} \text{ loops} \\ \frac{L_1}{k_{bat}} & \text{for } \bar{i}_{bat} \text{ loop} \end{cases}$$

3.1.2 Voltage loops regulation

To meet the control objectives, the same procedure adopted for the current-loop regulation in Subsection 3.1 is applied. Based on Eqs. (1) and (3), the following control laws are obtained:

$$
\begin{aligned}
\bar{i}_0^* &= \bar{i}_{pv} - k_{p_{pv}}(\bar{v}_{pv}^* - \bar{v}_{pv} + k_{i_{pv}}\int(\bar{v}_{pv}^* - \bar{v}_{pv})dt), && (12)\\
\bar{i}_{gq}^* &= \frac{1}{v_{gq}}\left(\bar{v}_{pv}\bar{i}_{pv} - \bar{v}_{bat}\bar{i}_{bat} - k_{p_{dc}}(e_{dc} + k_{i_{dc}}\int e_{dc}dt)\right), && (13)
\end{aligned}
$$

where $k_{p_{dc}}$, $k_{p_{pv}}$, $k_{i_{dc}}$, $k_{i_{dc}}$ are controllers' proportional and integral gains, and $e_{dc} = \bar{v}_{dc_{ref}}^2 - \bar{v}_{dc}^2$ is the voltage tracking error for DC-link regulation. The corresponding closed-loop transfer function is written as follows:

$$Hv(s) = \frac{1 + \frac{2\zeta}{\omega_0}s}{1 + \frac{2\zeta}{\omega_0}s + \frac{1}{\omega_0^2}s^2} \tag{14}$$

The controllers bandwidth ω_0 and damping coefficient ζ are given by th 2 table.

Table 2. The expressions of ω_0 and ζ

Loop	ω_0	ζ
$\bar{v}_{pv}$	$\sqrt{\frac{k_{i_{pv}} k_{p_{pv}}}{C_{pv}}}$	$\frac{1}{2}\sqrt{\frac{k_{p_{pv}}}{k_{i_{pv}} C_{pv}}}$
$\bar{v}_{dc}$	$\sqrt{\frac{2k_{p_{dc}} k_{i_{dc}}}{C_{dc}}}$	$\sqrt{\frac{k_{p_{dc}}}{2k_{i_{dc}} C_{dc}}}$

3.2 PI Controller Tuning via Reinforcement Learning (RL-PI)

PI control remains common in power electronic converters owing to their uncomplicated formulation and low implementation effort. However, determining the optimal gain values k_p, k_i remains a challenge, particularly under varying operating conditions. In this work, as shown in figure 2, we propose the use of an RL agent to tune PI gains online, enabling adaptive control in a disturbed system.

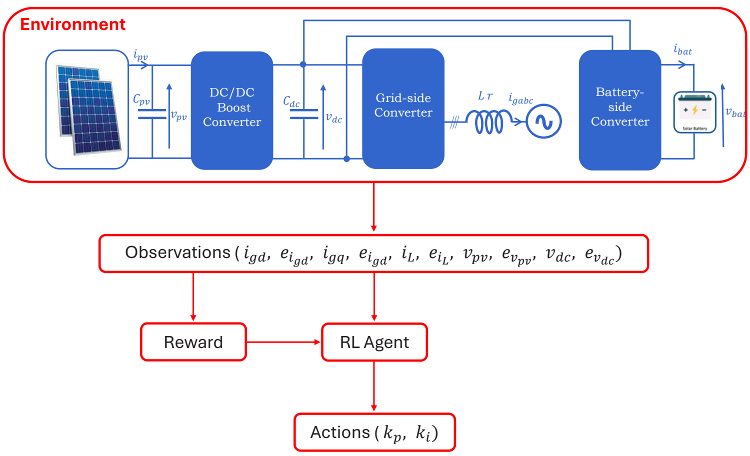

Figure 2. DRL frame work illustrating agent-environment interactions.

3.2.1 Problem Formulation

The tuning task is modeled as a continuous action reinforcement learning problem. The environment corresponds to the control system in which the PI controller regulates a target variable ($\bar{i}_0$, $\bar{i}_{gd}$, $\bar{i}_{gq}$, $\bar{v}_{pv}$ or $\bar{v}_{dc}$). The RL agent observes the current or voltage state of the system and outputs the controller gains (k_p, k_i) in real time.

- **Observation:** The observation vector includes features that characterize the regulation performance, such as the instantaneous error $e(t)$ for each loop, its derivative $\dot{e}(t)$, the system output $y(t)$, and optionally, the control signal $u(t)$. This multidimensional representation allows the agent to capture the system dynamics effectively and adjust the PI parameters accordingly.
- **Action Space:** The action is defined as a two-dimensional vector $\mathbf{a}(t) = [K_p(t), K_i(t)]^\top$, with each gain constrained within predefined bounds to ensure system stability and prevent excessive control efforts. These bounds are determined based on prior controller knowledge and physical limitations of the converter and actuators.

- **Reward Function:** The reward is designed to minimize tracking error while penalizing excessive control effort. A typical formulation is:

$$r(t) = \begin{cases} 1 - |e(t)|^2, & \text{if } |e(t)| \leq 0.001 \\ 0.01 - |e(t)|^2, & \text{if } 0.001 < |e(t)| \leq 0.01 \\ 0.001 - |e(t)|^2, & \text{if } 0.01 < |e(t)| \leq 0.1 \\ -5|e(t)|^2, & \text{if } 0.1 < |e(t)| \end{cases} \tag{15}$$

where α and β are weighting coefficients.

3.2.2 Learning Algorithm and Training Strategy

Given the continuous nature of the action space and the requirement for stable policy updates, the Twin Delayed Deep Deterministic Policy Gradient (TD3) algorithm was adopted. The RL agent is implemented using MATLAB/Simulink's RL toolbox. It interacts with a Simulink model of the system via the `rlSimulinkEnv` interface. At each sampling instant, the agent computes a new set of PI gains, from which the control signal is computed:

$$u(t) = k_p(t)e(t) + k_i(t) \int e(t)\, dt \tag{16}$$

Each training episode simulates the system over a fixed time horizon under varying irradiance. The agent is trained to maximize cumulative reward.

3.2.3 Validation and test

After training convergence, the learned agent is subjected to a validation and testing phase to assess its generalization capability and robustness under unseen conditions. During validation, the agent operates on a set of scenarios not used during training, such as different irradiance levels. The PI gains generated by the agent are fixed throughout each test episode to assess closed-loop performance in terms of convergence time, peak deviation, residual steady-state error, and disturbance attenuation capability. Additionally, the agent's response is compared against conventional and fixed-parameter PI controllers to highlight the benefits of adaptive tuning. This step ensures that the trained policy performs reliably in realistic operational conditions beyond the training environment.

3.3 LADRC

In LADRC, model uncertainties and external perturbations are grouped into a total disturbance, which is reconstructed online by an extended state observer (ESO). The corresponding control structure is depicted in Figure 3.

We had observed the same behavior and dynamic for all current loops, including $\bar{i}_0$, $\bar{i}_{gd}$, and $\bar{i}_{gq}$, as well as for the control of voltage loops $\bar{v}_{pv}$ and $\bar{v}_{dc}$. To summarize, the analysis is conducted by demonstrating the control strategy for a single inner loop, since the conclusions remain valid for all other loops.

The current and voltage dynamics are written in the following generic first-order form:

$$\dot{x} = f_b + bu \tag{17}$$

The definitions of x, f_b, b, and u for the different subsystems are reported in Table 3.

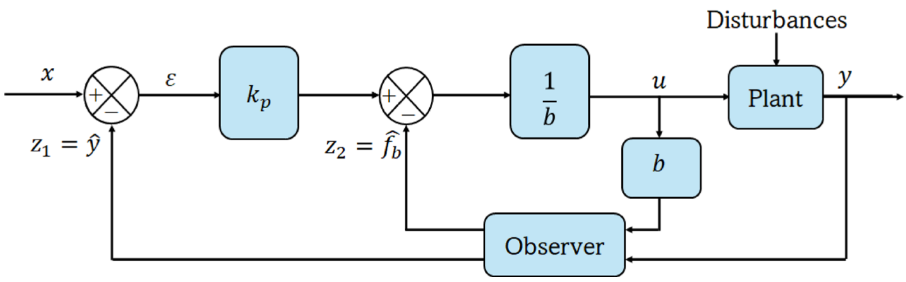

Figure 3. General structure of the first-order LADRC scheme.

Table 3. Expressions of x, f_b, b and u for each sub-system

x	f_b	b	u
$\bar{i}_0$	$\frac{1}{L_0}(\bar{v}_{pv} - \bar{v}_{dc})$	$\frac{1}{L_0}$	u_0
$\bar{i}_{gd}$	$\omega\bar{i}_{gq} - \frac{1}{L}r\bar{i}_{gd}$	$\frac{\bar{v}_{dc}}{2L}$	u_d
$\bar{i}_{gq}$	$-\omega\bar{i}_{gd} - \frac{1}{L}(r\bar{i}_{gq} + v_{gq})$	$\frac{\bar{v}_{dc}}{2L}$	u_q
$\bar{v}_{pv}$	$\frac{1}{C_{pv}}\frac{di_{pv}}{dt}$	$-\frac{1}{C_{pv}}$	$\bar{i}_0^*$
$\bar{v}_{dc}^2$	$\frac{2}{C_{dc}}(\bar{v}_{pv}\bar{i}_0 - v_{bat}\bar{i}_{bat})$	$-\frac{2\bar{v}_{gq}}{C_{dc}}$	$\bar{i}_{gq}^*$

To estimate and reject the lumped disturbance, the observer is constructed from the augmented representation:

$$\begin{cases} \dot{x} = f_b + bu \\ \dot{z_2} = \dot{\hat{f}_b} \end{cases} \tag{18}$$

Since the current dynamics are assumed to be considerably faster than the voltage dynamics, separate observers are assigned to the inner and outer loops. They are expressed as:

$$\begin{cases} \dot{\hat{x}} = \hat{z}_2 + bu - \beta_{i_1}(\hat{x} - x) \\ \dot{\hat{z}}_2 = -\beta_{i_2}(\hat{x} - x) \end{cases} \tag{19}$$

$$i = \begin{cases} c & \text{for current loops} \\ v & \text{for voltage loops} \end{cases}$$

The coefficients β_{i1} and β_{i2} set the observer response speed and are selected from the observer bandwidth ω_i as follows:

$$\begin{cases} \beta_{i_1} = 2\omega_i \\ \beta_{i_2} = \omega_i^2 \end{cases} \tag{20}$$

The control input u is therefore expressed as:

$$u = \frac{k_i(\hat{x} - x) - z_2}{b} \tag{21}$$

where k_i is a tuning parameter selected to separate the observer and controller dynamics.

Table 4. Controllers Parameters

ADRC	PI
$\omega_i = 2 \times 10^4$	$k_0 = 1000$, $k_{p_{pv}} = 0.089$
$\omega_o = 2 \times 10^3$	$k_{i_{pv}} = 222.2$, $k_{p_{dq}} = 15$
$k_i = 1000$	$k_{i_{dc}} = 23, 31$, $k_{p_{dc}} = 0.12$
$k_o = 400$	$k_{bat} = 1000$

4 Simulation Results

The configuration shown in Figure 4 is simulated in MATLAB/Simscape. The photovoltaic generator includes eight parallel branches, each formed by eleven modules connected in series. At an irradiance of 1000 W/m^2 and a temperature of 25°C, it produces 30.79 kW at 423.5 V. The boost converter raises this voltage and supplies the regulated DC link. The grid-side inverter subsequently generates a three-phase voltage of 220 V RMS. A 200 V battery rated at 20 kW is connected to the system for energy storage. After satisfying the battery charging requirement, the available surplus PV power is delivered to the utility grid.

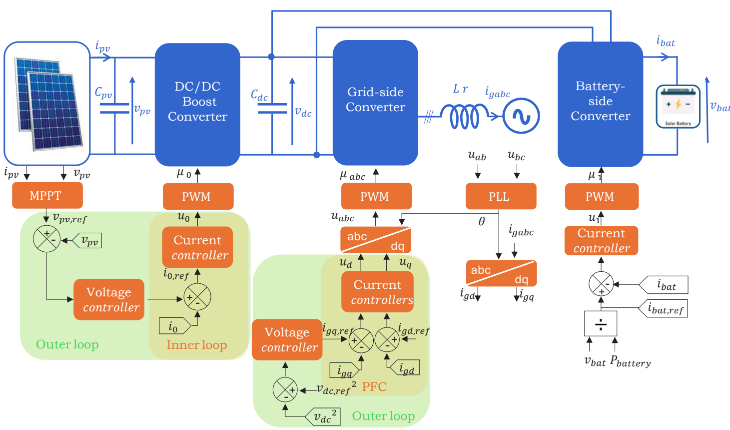

Figure 4. Block diagram of the complete control system.

4.1 PV system parameters description

Variable irradiance profiles are considered in the simulations, while maximum power point tracking is performed using the P&O method. The selected system values are $C_{pv} = 0.2$ mF, $L_0 = L_1 = L = 1$ mH, $C_{dc} = 5$ mF, and $r = 0.1$ mΩ. The controller tuning parameters are reported in Table 4.

4.2 Tracking test

For this test, the temperature and solar irradiance are fixed at 25°C and 1000 W/m^2, respectively. The DC-link voltage reference $v_{dc\text{ref}}$ is increased from 700 V to 750 V at $t = 0.3$ s, and restored to 700 V at $t = 0.4$ s.

The responses reported in Figure 5 indicate that the three controllers accurately follow the imposed DC-link voltage changes with negligible overshoot. The grid currents also retain a sinusoidal waveform and remain nearly aligned with the grid voltage, resulting in a power factor close to unity.

The ADRC controller demonstrates a well-damped response, with no observable overshoot, and a fast settling time. The PI compensator shows a slower response and a slight overshoot, reflecting the limitations of fixed-parameter tuning. In contrast, the PI-RL controller presents the fastest transient response among all tested strategies, achieving setpoint tracking without overshoot. This suggests that reinforcement learning has effectively optimized the PI parameters to enhance both dynamic performance and stability, outperforming conventional tuning methods.

figure 6 shows that the components i_{gd} and i_{gq} of the current follow their references. This figure shows that the ADRC controller offers a good compromise between overshoot and convergence speed.

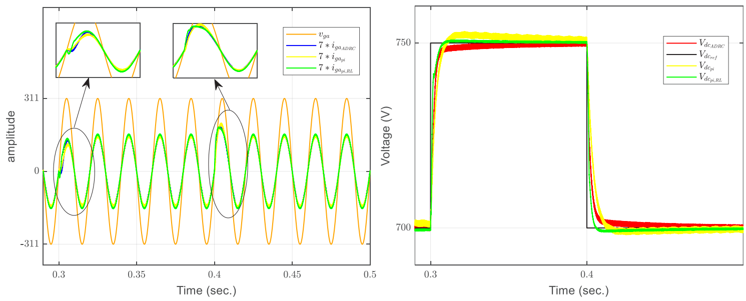

Figure 5. Tracking test: DC link voltage and Phase (a) voltage and current.

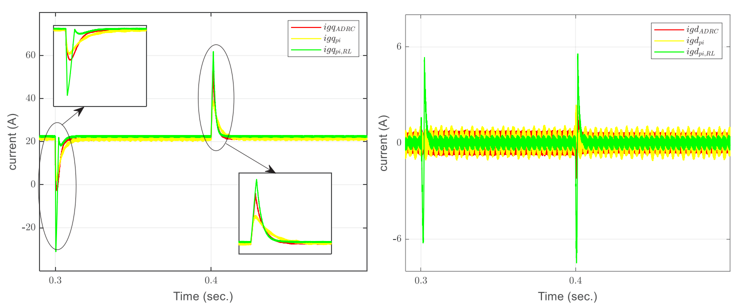

Figure 6. Tracking test: d-axis and q-axis components of grid current.

4.3 Robustness test

In this test, the temperature is maintained at 25°C, whereas the irradiance is reduced from 1000 W/m^2 to 400 W/m^2 at $t = 0.25$ s, before being restored to 1000 W/m^2 at $t = 0.6$ s.

During the irradiance drop, the PV array no longer supplies enough power to meet the battery charging requirement. The missing power is therefore drawn from the grid. This change from grid injection to grid consumption can be observed in Figure 7, where the grid current becomes opposite in phase to the grid voltage.

Once the irradiance returns to 1000 W/m^2, the PV power increases again. The battery continues to charge, while the remaining generated power is delivered to the grid.

Figure 8 verifies the power balance of the overall system. The generated photovoltaic power P_{pv} is distributed between the battery charging power and the grid power, denoted by $P_{consumed}$. The same figure also shows that the reactive power remains regulated around zero, confirming operation at unity power factor.

Figure 9 shows that the battery current accurately tracks its reference value, thereby ensuring constant-current charging.

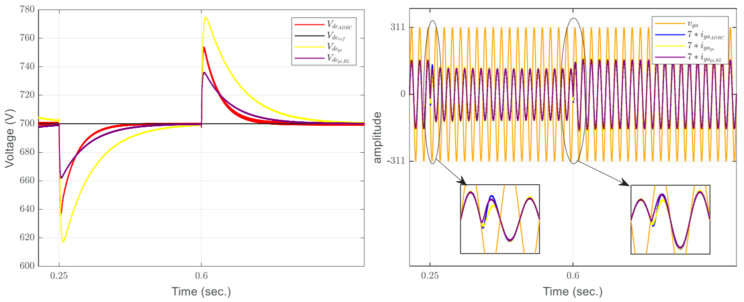

Figure 7. Robustness test under irradiance disturbances: DC link voltage and Phase (a) voltage and current.

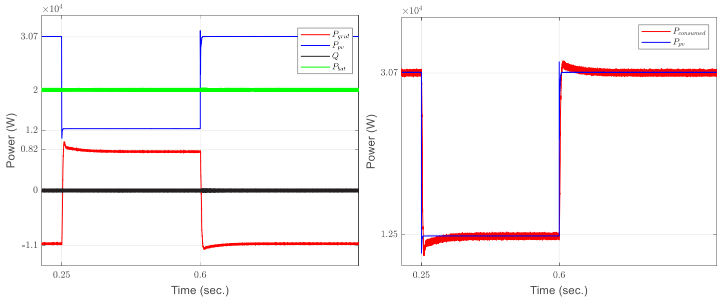

Figure 8. Power variation and conservation under irradiance disturbances.

4.4 Comparison

The closed-loop responses obtained with the proposed controllers show satisfactory reference tracking and regulation performance. As illustrated in Figure 10, the PV-array voltage converges to the optimal value determined by the MPPT algorithm. The same figure indicates that the boost-converter input current tracks the reference generated by the outer PV-voltage control loop. This figure highlights the impact of the control strategy on the regulation of v_{pv} which is directly linked to the effectiveness of the MPPT process. It is observed that the ADRC controller maintains the PV voltage very close to the optimal MPPT voltage. In contrast, the PI-RL controller provides the most accurate and stable tracking of the current

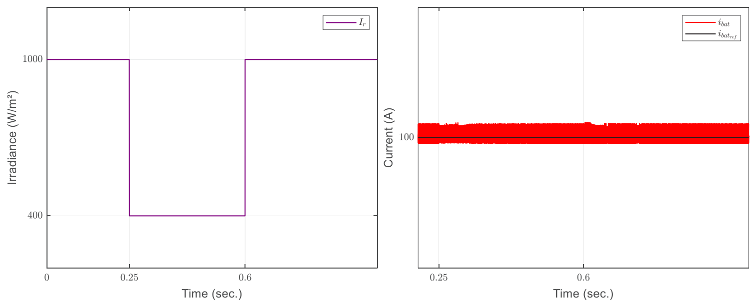

Figure 9. Irradiance disturbance and battery's charging current.

reference i_{Lref}, with minimal oscillations and a fast convergence following changes in irradiance.

figure 7 shows that the injected currents are sinusoidal with a unitary power factor. It also shows that The PI-RL controller demonstrates superior performance in all subplots: the grid current $i_{ga_{pi,RL}}$ tracks the reference waveform smoothly without the need for a significant transient regime, confirming the robustness and optimality of PI-RL control. The DC-link voltage v_{dc} is regulated at its reference value even with changing climatic conditions. The PI-RL controller achieves the fastest convergence to the reference with minimal undershoot and overshoot, ensuring a highly damped and stable response. The classical PI presents significant overshoot and slow settling, while ADRC offers a compromise with slightly improved damping but slower recovery than the PI-RL.

figure 11 shows that the current $i_{gq_{pi,RL}}$ reaches its steady-state the fastest with no overshoot, the $i_{gd_{pi,RL}}$ component shows the narrowest bandwidth, indicating effective suppression of unnecessary oscillations.

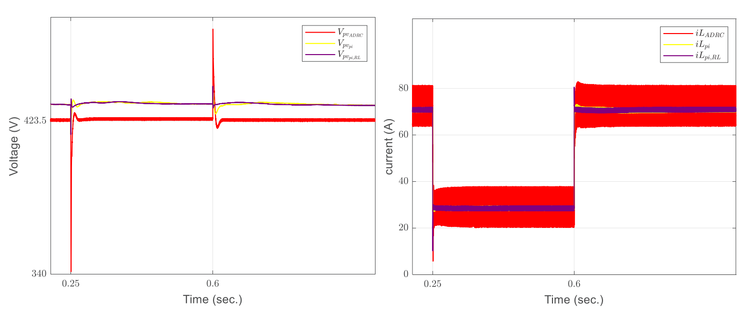

Figure 10. Robustness test under irradiance disturbances: PV voltage and boost chopper current.

5 Conclusion

This work investigated the control of a grid-connected photovoltaic system equipped with battery storage using three approaches: conventional PI, Linear ADRC, and a reinforcement-learning-based PI controller. Their performance was assessed in terms of maximum PV power extraction, unity power factor operation, DC-link voltage stabilization, and battery

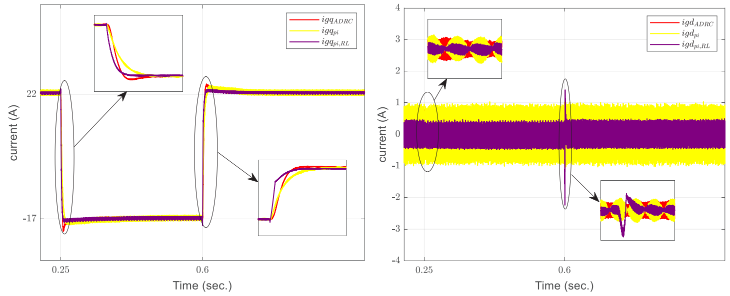

Figure 11. Robustness test under irradiance disturbances: d-axis and q-axis components of grid current.

charging regulation. The simulation results confirm that the three methods satisfy the required control objectives. Nevertheless, LADRC and PI-RL provide better performance than the conventional PI controller, particularly regarding robustness, settling time, overshoot reduction, and reference tracking.

References

1. A. Q. Al-Shetwi, I. Z. Abidin, K. A. Mahafzah and M. A. Hannan, Feasibility of future transition to 100% renewable energy: Recent progress, policies, challenges, and perspectives. Journal of Cleaner Production **000**, 143942 (2024). https://doi.org/10.1016/j.jclepro.2024.143942
2. K. R. Abbasi, Q. Zhang, I. Ozturk, R. Alvarado and M. Musa, Energy transition, fossil fuels, and green innovations: Paving the way to achieving sustainable development goals in the United States. Gondwana Research **130**, 326–341 (2024). https://doi.org/10.1016/j.gr.2024.02.005
3. M. Morey, N. Gupta, M. M. Garg and A. Kumar, A comprehensive review of grid-connected solar photovoltaic system: Architecture, control, and ancillary services. Renewable Energy Focus **45**, 307–330 (2023). https://doi.org/10.1016/j.ref.2023.04.009
4. A. Q. Al-Shetwi, M. A. Hannan, K. P. Jern, M. Mansur and T. M. I. Mahlia, Grid-connected renewable energy sources: Review of the recent integration requirements and control methods. Journal of Cleaner Production **253**, 119831 (2020). https://doi.org/10.1016/j.jclepro.2019.119831
5. E. Elbouchikhi, G. Feld, Y. Amirat, M. Benbouzid and F. Le Gall, Design and experimental implementation of a wind energy conversion platform with education and research capabilities. Computers & Electrical Engineering **85**, 106661 (2020). https://doi.org/10.1016/j.compeleceng.2020.106661
6. H. Katir, A. Abouloifa, K. Noussi, I. Lachkar, A. El Aroudi, M. Aourir, F. El Otmani and F. Giri, Fault Tolerant Backstepping Control for Double-Stage Grid-Connected Photovoltaic Systems Using Cascaded H-Bridge Multilevel Inverters. IEEE Control Systems Letters **6**, 1406–1411 (2022). https://doi.org/10.1109/LCSYS.2021.3095107
7. D. A. Zambrano-Prada, A. El Aroudi, O. López-Santos, L. Vázquez-Seisdedos and L. Martínez-Salamero, Adaptive Sliding Mode Control of a Boost Converter With Unknown Constant Power Load. IEEE Access **13**, 33714–33732 (2025). https://doi.org/10.1109/ACCESS.2025.3543659

8. E. Elbouchikhi, A. B. El Moubarek, A. Abouloifa, A. El Aroudi and M. Benbouzid, Active disturbance rejection control for four-wire inverters in standalone renewable resources-based microgrid — islanded microgrids ADRC-based control. ISA Transactions **156**, 290–306 (2025). https://doi.org/10.1016/j.isatra.2024.11.006
9. M. Ahmed, I. Harbi, R. Kennel, J. Rodríguez and M. Abdelrahem, Maximum power point tracking-based model predictive control for photovoltaic systems: Investigation and new perspective. Sensors **22**(8), 3069 (2022). https://doi.org/10.3390/s22083069
10. M. A. R. Shafei, D. K. Ibrahim and M. Bahaa, Application of PSO tuned fuzzy logic controller for LFC of two-area power system with redox flow battery and PV solar park. Ain Shams Engineering Journal **13**(5), 101710 (2022). https://doi.org/10.1016/j.asej.2022.101710
11. J. N. Bhanutej, G. G. Kumar, N. Kalahasthi and K. S. Mahalakshmi, Analysis and Design of Reliable Converter Topology for Grid Connected PV Systems with ANN Controller. In: 2023 3rd International Conference on Smart Generation Computing, Communication and Networking (SMART GENCON), pp. 1–5 (2023). https://doi.org/10.1109/SMARTGENCON60755.2023.10442287
12. E. O. Arwa and K. A. Folly, Reinforcement Learning Techniques for Optimal Power Control in Grid-Connected Microgrids: A Comprehensive Review. IEEE Access **8**, 208992–209007 (2020). https://doi.org/10.1109/ACCESS.2020.3038735
13. C. Yanarates and Z. Zhou, Design and Cascade PI Controller-Based Robust Model Reference Adaptive Control of DC-DC Boost Converter. IEEE Access **10**, 44909–44922 (2022). https://doi.org/10.1109/ACCESS.2022.3169591
14. M. Mahazabeen, A. J. Abianeh, S. Ebrahimi and F. Ferdowsi, Performance Evaluation of an RL-Aided DAB-Based EV Charger Control. In: 2022 North American Power Symposium (NAPS), pp. 1–5 (2022). https://doi.org/10.1109/NAPS56150.2022.10012228